Multiple Dendrite Tip Tracking for In-Situ Directional Solidification: Experiments and Comparisons to Theory

T. Hughes[a], A. J. Robinson[a], S. McFadden[b*]

[a]Department of Mechanical, Manufacturing and Biomedical Engineering, Trinity College Dublin, Ireland

[b]School of Computing, Engineering, and Intelligent Systems, Ulster University, Magee Campus, Londonderry, Northern Ireland BT487JL, United Kingdom. (permanent address)

Corresponding Author: s.mcfadden2@ulster.ac.uk +44 28 7167 5652

Keywords: Crystal growth, Directional solidification, In situ, Microstructure formation, Image analysis

Abstract

Directional solidification experiments of transparent alloy systems typically show multiple dendrites, a forest of dendrites, growing with preferential alignment. At the length scale of centimetres, an experiment could have hundreds of observable dendrites. Analysis of every dendrite would be laborious and practically difficult to implement. Hence, low numbers of dendrites are routinely selected for analysis as they are assumed to be representative of the growth conditions. Hence, many dendrites go without being analysed. Here, a bespoke experimental apparatus with a novel computer vision algorithm is presented that automatically detects and simultaneously tracks multiple columnar dendrite tips from in-situ video data of directional solidification. The benefits of the algorithm are demonstrated with an application to an experimental test case with the transparent alloy system Neopentyl Glycol-35wt.%D-Camphor (NPG-35wt.%DC). Comparisons of dendrite tip velocity and undercooling measurements with microgravity experimental results from the literature showed notable differences. The current terrestrial data showed similar growth rates but at lower undercoolings (by factors in the range of 0.41 to 0.68) to that measured in the microgravity experiments. Comparisons were made to the classical Lipton-Glicksman-Kurz (LGK) model and to a modified LGK model adapted with a finite diffusional boundary layer theory to account for convection effects. The modified LGK model showed good agreement for boundary layers between 2.5 and 7.0μm. An oscillatory component to the tip velocity was observed between adjacent columnar dendrites. Video data of columnar dendritic growth augmented with tip velocity vectors are presented. The tip tracking algorithm is beneficial as, with 385 dendrite tips tracked, it provides statistical and qualitative insights that are otherwise difficult to reconcile using traditional methods.

1 Introduction

Dendrites are one of the most common crystal growth morphologies found in technologically important alloys. The evolution of dendritic morphologies during solidification play an important role in the quality and material properties of as-cast components. In-situ optical and x-ray radiographic investigations have deepened knowledge and understanding of the fundamental physical phenomena of solidification processes and have provided benchmark data for model validation (see reviews [1–5]). However, quantitative data extraction from in-situ video sequences is laborious and time-consuming. Moreover, manual tracking of crystals during solidification experiments, which can consist of thousands of frames with hundreds of columnar or equiaxed crystals, makes manual tracking practically difficult. Thus, much information available in the video data can remain unquantified. Several investigators have integrated computer vision and image processing methodologies into their experimental workflows for extracting quantitative data. Examples include the characterisation of nucleation events [6], the measurement of equiaxed area [7] and volume fractions [8,9], the tracking of growth fronts [10–12], the measurement of solute profiles [13–17], and the detection of dendrite centres [18–20]. While there are methodologies to track equiaxed crystal nucleation, volume fraction and position, there is no equivalent automatic method for columnar dendrite tip tracking within in-situ video data. This manuscript presents a newly developed computer vision algorithm for automatically detecting and tracking multiple columnar dendrite tips simultaneously using in-situ video data of directional solidification obtained from a bespoke experimental apparatus. The algorithm works by defining a contour of the columnar front for a given frame, similar to the envelope used in mesoscopic modelling and then clustering local maxima of contours into data groups associated with individual dendrites. In this investigation, up to 97 tips have been tracked in a given video sequence and, in total, 385 dendrites were tracked over 6 experiments. The data gathered here will be useful for analytical and numerical model validation.

The Ivantsov solution for steady-state thermal diffusion of an isothermal parabolic dendrite underpins classical dendrite growth theory [21,22]. Lipton, Glicksman and Kurz [23] coupled Ivantasov's transport solution with marginal stability theory [24], providing a fully determined solution and accounting for constitutional undercooling. The LGK model, which assumes a low Peclet number, was shown to agree well with microgravity experiments (dendritic growth in succinonitrile) [25] and has since been widely accepted. Nevertheless, the LGK diffusion-based solution is not consistent with terrestrial experimental data at low undercooling due to buoyancy-driven convection [26,27]. Several models have been developed to account for thermosolutal convection [28–33]; however, the well-documented effects of melt convection on dendrite growth [34] remains

a challenge [3]. Recent microgravity experiments with transparent alloys of Neopentyl Glycol and (D)Camphor (NPG-DC) provided in-situ data for diffusion-dominated dendritic growth in the transparent binary alloy [11,35]. In light of the recent microgravity experiments conducted in the NPG-DC system, this contribution aims to provide complementary terrestrial data for the NPG-DC system combined with a new computer vision algorithm for automatic identification and tracking of columnar dendrite tips.

The objectives are as follows: (a) to present a new computer vision algorithm for tracking columnar dendrite tip velocities from in-situ footage of directional solidification (b) to provide complementary terrestrial data for the columnar dendrite tip velocity versus undercooling relationship (especially for low undercooling, data which is currently lacking), and (c) to compare the terrestrial results of columnar dendrite tip velocity and undercooling with microgravity data and with theoretical models found in the literature.

2 Methodology

An overview of the experimental apparatus and procedure is provided, followed by detailed descriptions of the tip tracking algorithm. Readers may refer to [10] for more information on the experimental setup, control and measurement. The tip tracking algorithm is used to process the in-situ image and video data to detect and track the position, velocity, and orientation of multiple columnar dendrite tips as shown, by way of example, in Fig. 1.

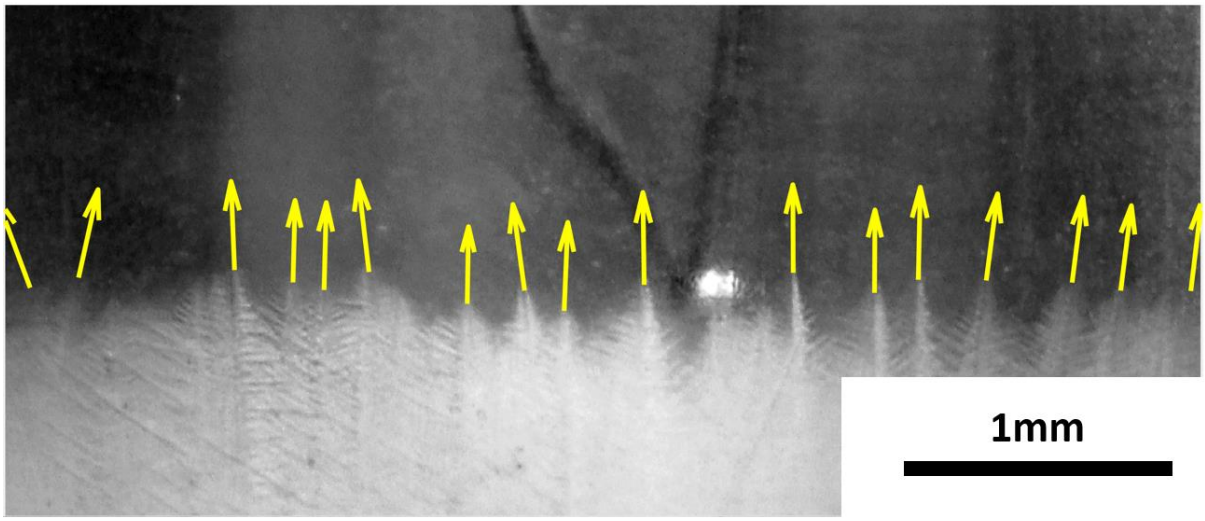

Fig. 1. An image from an in-situ video sequence of directional solidification showing a representative result from the automatic tracking algorithm (velocity vectors). The columnar front is shown crossing an internal thermocouple used for tip undercooling measurements.

2.1 Apparatus

The experimental apparatus is comprised of a transparent sapphire crucible combined with a thermal regulation system to give hot and cold regions. The thermal regulation facilitates controlled temperature gradient, G, cooling rate, $\dot{T}$, and, hence, liquidus isotherm speed, v_L. Sapphire was chosen as the crucible material because it is optically transparent, allowing optical visualisation of the top of the mushy zone and, due to its high thermal conductivity (40 W/mK), facilitates heat transfer to and from the material with low temperature difference (< 1 K) across the crucible wall.

Fig. 2 shows a technical illustration of the experimental facility. It consists of a vertical sapphire crucible of 450mm length, with an inner diameter of 8mm and an outer diameter of 10mm. An Ohmic heater in the upper section consists of a coiled nichrome wire connected with a power supply (Automatik EA-PSI-8360-10T DC). The nichrome wire is wrapped tightly around the outer tube wall with a thermally conductive silicone layer to provide adequate thermal contact and electrical isolation. A dedicated computer system controls T_H using a power supply with an EA-IF-U1 interface card and proportional-integral control loop in LabView®. Heat is extracted from the lower section with a 170mm long tube-and-shell type heat exchanger. A Julabo A40 precision chiller in series with a pump supplies chilled water to the heat exchanger with initial controlled setpoints followed by controlled cooling at a rate of $\dot{T}_C$ within the range of 0.2 to 0.6 K/min being possible. Two thermocouples that pass into the heat exchanger are embedded into the wall of the sapphire crucible. These two thermocouples provide temperature measurements of the crucible wall inside the heat exchanger, the average of which is designated as T_C. T_H is controlled to be ramped down at the same cooling rate as $\dot{T}_C = dT_C/dt$ in order to maintain a constant temperature gradient $G = (T_H - T_C)/z_{HC}$, with z_{HC} being the axial distance between thermocouples, T_H and T_C. Thus, for a fixed G specified by the user, the setpoint T_H for the controller is calculated as:

$$T_H = T_C + Gz_{HC} \quad (1)$$

Pairs of 0.5mm diameter blind holes have been drilled at several heights along the crucible wall into which T-type thermocouples have been inserted with an essential amount of thermal adhesive. Fig. 2 shows four temperature measurement locations designated as T_H, T_{A1}, T_{A2}, and T_C. Each location has a pair of thermocouples at the given height where the average temperatures of each diametrically-opposed thermocouples pair are used. T_C and T_H are controlled to set the temperature gradient and cooling rate in the baffle zone (as described previously), while T_{A1} and T_{A2} are used to provide the measured temperature gradient, G, given the known vertical distance between them of 6.5mm. An optional temperature probe can be passed vertically downwards into the crucible through an O-ring seal on the upper end-cap. The temperature probe consists of 3mm diameter

stainless steel tube housing with an 80 µm T-type thermocouple with Teflon® sheath that extends 30mm from the stainless steel tube.

A Canon EOS 200D camera with a Navitar 3x – 10x zoom lens is mounted with its optical axis orthogonal to the observation window. The synchronisation of the camera and computer clocks facilitates simultaneous measurement of the temperatures and solidification parameters combined with in-situ microscopic videography of the solidification. As solidification at low undercooling is a relatively slow process, images are captured at a frame rate of 0.5 fps. The camera provides the original images in JPEG format and PNG compression is used for all subsequent storage.

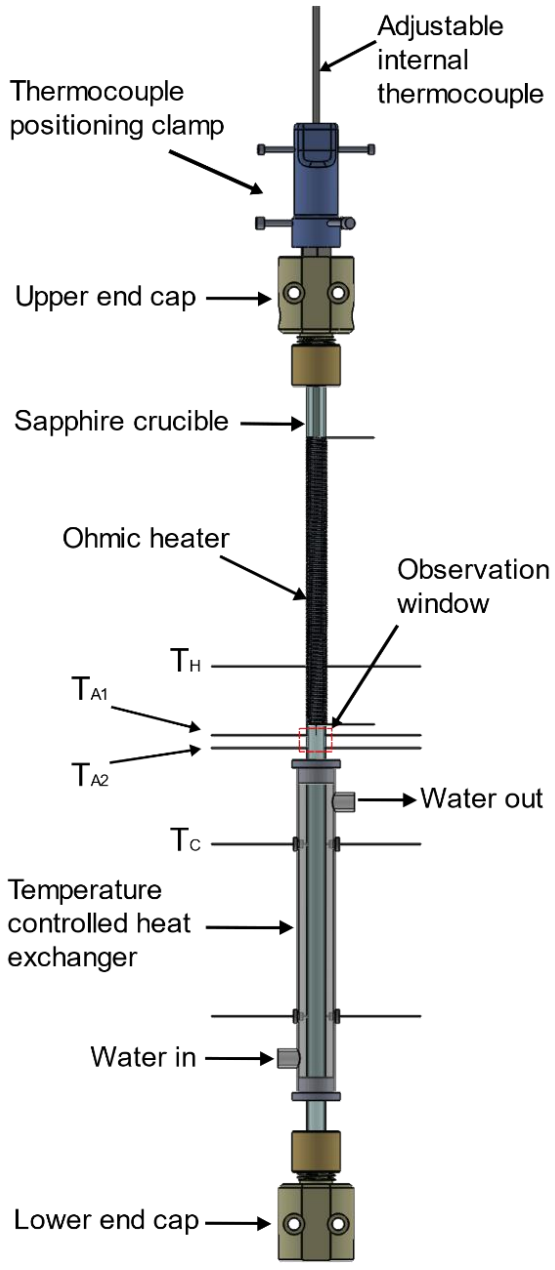

Fig. 2. Technical illustration of apparatus with the observation window shown in the centre

2.2 Procedure

This work investigated directional solidification occurring vertically upward from the cooled solid zone following initiation of a controlled ramp-down of set point temperatures T_C and T_H. To investigate the relationship between columnar dendrite tip velocity and undercooling, a total of six tests were conducted with different isotherm velocities by varying the setpoint cooling rates, $\dot{T}_H$ and $\dot{T}_C$, and temperature gradient, G. In each test, the newly developed computer vision algorithm automatically tracked the columnar dendrite tips and, when dendrites crossed the internal thermocouple, this provided instantaneous measurement of the columnar dendrite tip velocity with undercooling.

As NPG is hygroscopic, the transparent alloy was prepared in a sealed glove box under Argon atmosphere (<5ppm H_2O). The batch consisted of 40.02g of neopentyl glycol, and 21.53g of (d)Camphor weighed using a KERN Analytical balance (0.1mg uncertainty). The materials were heated and mixed in an Erlenmeyer flask with a perforated subaseal® septum on top to contain sublimated materials and provide pressure compensation. The alloy was transferred from the glovebox in a high-temperature gas-tight glass syringe. The sapphire crucible was flushed with dry air, and the liquid NPG-35wt.%DC was injected through a Leur Lok valve on the lower end-cap (not shown). The crucible was then filled to the upper level of the Ohmic heater with an excess of argon from the glove box filling the remaining volume of the crucible above the heater.

For the present experiments, the test material in the crucible above the cooled heat sink region was brought into the liquid phase by increasing the Ohmic heater's temperature to 120°C. To ensure a homogenous initial composition in the liquid melt before any given test, the baffle zone was heated with a heat gun and the Ohmic heater was temporarily turned off to induce convective mixing for a period of 5 minutes. The set points on the thermocouple pairs T_H and T_C were then adjusted such that the solidification front was just below the observation window and maintained for at least 40 minutes to allow the solidification front to reach the liquidus isotherm, just inside the observation window. Two images of the solidification front were routinely captured five minutes apart and compared to confirm that the solidification front position was stationary. The adjustable internal thermocouple was manually traversed vertically downwards to the columnar front and clamped at the solidification front for two minutes to confirm the liquidus temperature recording. The probe was then brought back to the top of the observation window before commencing with directional solidification. At this point in any of the experiments, ramp down cooling was initiated, and optical imaging commenced. Progression of the mean dendrite tip velocity for each test was provided by

the computer vision algorithm and was used to confirm if the growth rate had achieved a steady state.

Table 1 lists the thermal processing parameters for the six experiments, which provided a corresponding range of isotherm speeds between 1.13 and 4.53 μm/s. The measured cooling rate from the internal thermocouple, $\dot{T}_i$, was recorded. The internal temperature gradient, G_i, was provided after a calibration correction as detailed in previous work [10]. The calibration correction equation used was $G_i=1.27G_e-0.22$, where G_e, is the measured temperature gradient on the wall of the sapphire crucible calculated using information from T_{A1} and T_{A2} and based on the spacing between the thermocouples. The relationship between G_i and G_e was established based on measurements during initial steady-state conditions; hence it does not account for transients introduced during solidification may also be a source of error in isotherm speed measurement. The thermophysical properties for the alloy are listed in table 2.

Table 1. Imposed solidification parameters

Test no.	$\dot{T}_i$ [K/min]	G_i [K/cm]
I	0.16	23.30 ± 2.36
II	0.30	23.58 ± 2.40
III	0.45	23.64 ± 2.40
IV	0.16	16.79 ± 2.26
V	0.30	16.55 ± 1.72
VI	0.45	16.57 ± 1.74

Table 2. Thermophysical properties

Property	Symbol	Value	Units	Ref.
Average Composition	C_0	35	[wt.%]	exp.
Liquidus Temperature	T_L	72.6	[°C]	exp.
Liquidus Slope	m_L	-1.65	[K/wt.%]	[11,36]
Equilibrium partition coefficient	k_0	0.086	[-]	[11,36]
Diffusivity of solute in liquid (at C_E=45.3wt.%)	D_L	9.7×10^{-11}	[m^2/s]	[37]
Gibbs-Thompson coefficient (at C_E=45.3wt.%)	Γ	7.8×10^{-8}	[Km]	[38]
Thermal conductivity in liquid and solid	k_L, k_S	0.12, 0.27	[W/mK]	[39]

2.3 Columnar tip tracking

The computer vision algorithm works by generating a contour at the top of the mushy zone for a given image of the video sequence (see Fig. 4 (c)). The contours consist of peaks and valleys around the columnar dendrites at the top of the mushy zone, similar to a grain envelope used in mesoscopic solidification modelling. Determination of local maxima from each contour yields a set of points, $\mathbf{p}_{ik}(x,y,t_i)$, which includes columnar tip positions. Fig. 3 summarises the sequence of steps in the columnar tip tracking algorithm. They comprise three main stages (i) pre-processing, (ii) contouring and (iii) tip-data extraction. Each stage is described next.

2.3.1 Pre-processing

At a given time, t, two high-resolution 8-bit grayscale images, denoted I_t and $\mathrm{I}_{t+\Delta t}$ (separated by a nominal time Δt), are selected for analysis. To preclude any vibrations arising in the video data, I_t and $\mathrm{I}_{t+\Delta t}$ are passed through an antishake algorithm that registers each frame to the first frame in the video sequence I_{t0}. The antishake algorithm detects feature points in a given frame using the MATLAB™ implementation of the minimum eigenvalue algorithm developed by Shi and Tomasi [40] and then matches them with feature points in I_{t0} to provide Euclidean image transformations when necessary. Automatic front-tracking (see previous work [10]) provides an average position of the columnar front, $\mathrm{y_f}$. Using $\mathrm{y_f}$, the algorithm crops input images to a height of $\mathrm{y_f} \pm \mathrm{h}$ and a width of approximately 6mm centred on the crucible vertical axis. The user nominally defines h based on experience or using trial and error for optimum results, typically 5% of the image height (rounded to the nearest integer pixel position). For test No. VI, h was set to 7% to capture the solidification front's broader range. When $\mathrm{y_f} \pm \mathrm{h}$ exceeds the image domain; the exceeding bound is reassigned at the top or bottom of the image as required. The cropped images, $\mathrm{I}_{c,t}$ and $\mathrm{I}_{c,t+\Delta t}$, are then passed onto the contouring stage of the algorithm.

Positions $\mathbf{p}_{ik}$ use two frames of reference, the intrinsic image coordinates and the world coordinates, which are indicated with subscripts p and w, respectively. The intrinsic image coordinates are defined by discrete pixel indices with column and row numbers corresponding to the x and y positions, respectively. Thus, the pixel position (1,1) is located at the centre of the image's upper-leftmost pixel with the y-axis pointing downwards [41]. A single reference on the first image, $\mathbf{p}_{\mathrm{ref,p}}$ and known width of the crucible, $\mathrm{w_w} = 1 \times 10^{-2}$m facilitated conversions from intrinsic image coordinates to world coordinates as follows:

$$\mathbf{p}_{\mathrm{w}} = \left(\frac{\mathrm{w_w}}{\mathrm{w_p}}\right)\left[(\mathrm{x_p} - \mathrm{x_{ref,p}})\mathbf{i} - (\mathrm{y_p} - \mathrm{y_{ref,p}})\mathbf{j}\right] \quad (2)$$

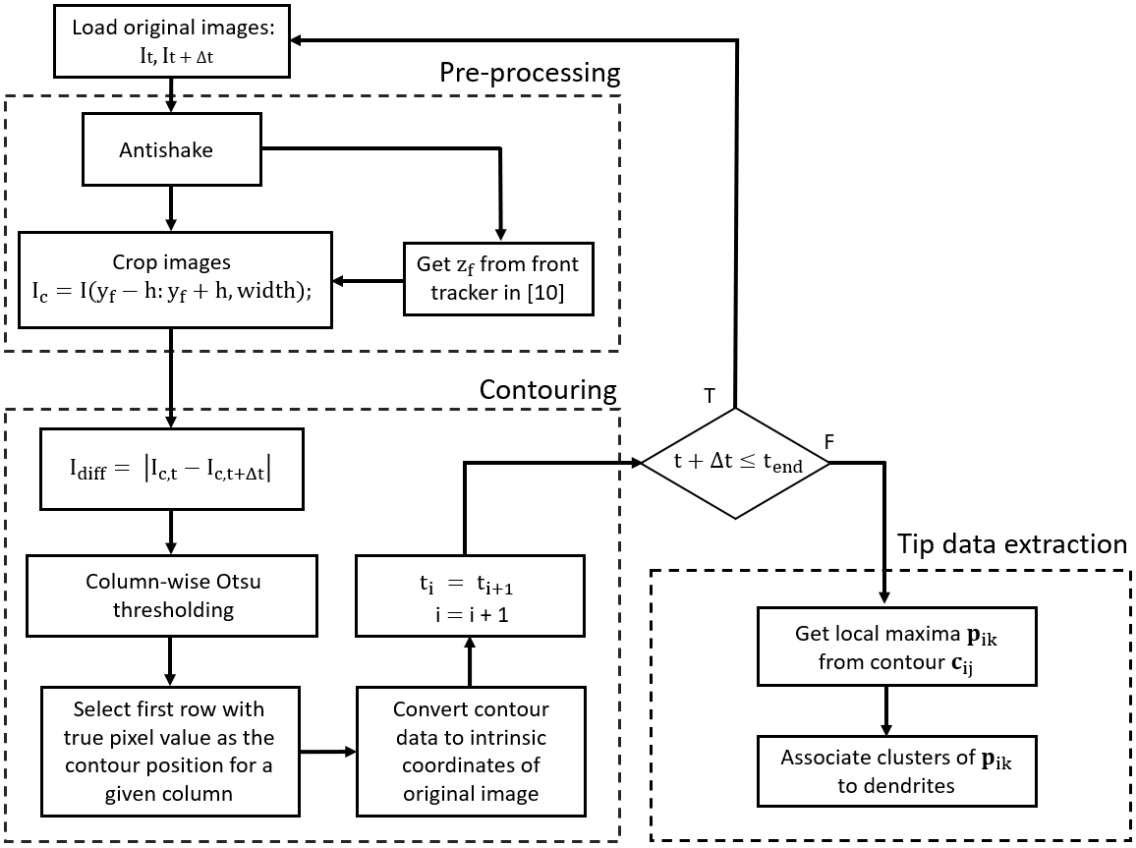

Fig. 3. Flow chart of columnar tip tracking algorithm

$\mathbf{p}_{ref,p}$ was manually selected at the height of T_{A2}, with x position corresponding to a 2mm inset from the left wall of the sapphire crucible (in line with the first column of the cropped images). Eq. (2) gives the position in the world reference frame from the ratio of the known width, w_w, in the world frame to the pixel width, w_p, in the image frame. Position data are nominally stored as intrinsic coordinates of original input images and converted using Eq. (2) as required. For clarity, references to the position are herein described in world coordinates, i.e. with origin corresponding to $\mathbf{p}_{ref}$ and the y-axis pointing vertically upwards.

2.3.2 Contouring

Fig. 4 (a) to (c) illustrate the steps involved in contouring the solidification front. Firstly, background removal by frame differencing, using Eq. (3), provides an image that highlights newly formed solid between two frames:

$$I_{diff} = |I_{c,t+\Delta t} - I_{c,t}| \quad (3)$$

Fig. 4 (a) shows an example of the resulting 8-bit grayscale image I_{diff} (contrast stretched for visualisation). Taking smaller fixed Δt reduces the presence of unwanted artefacts and improves the detail of the columnar front in I_{diff} for use in contouring.

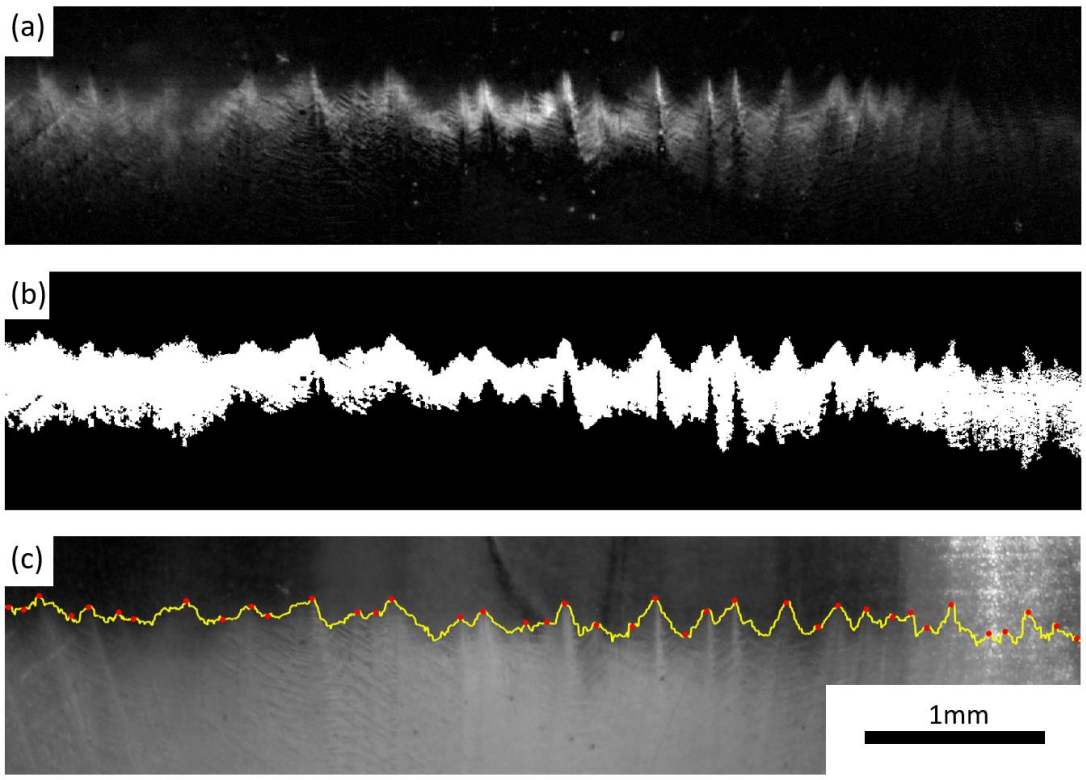

Fig. 4. Images illustrating steps in the contouring phase of the tip tracking algorithm: (a) absolute difference between two successive images, denoted I_{diff}, (b) binary image output from column-wise Otsu thresholding of I_{diff}, and (c) cropped input image $I_{c,t+\Delta t}$ with resulting contour overlay (yellow) delineating the liquid and mushy zones. Local maxima are shown as red dots.

Column-wise Otsu thresholding of I_{diff} generates a binary image used to determine the solidification front's contour (see Fig. 4 (b)). The Otsu algorithm automatically selects an optimal threshold grey-level for separating input pixels into two classes by minimising the weighted sum of within-class variances [42]. Otsu thresholding works well for input images with a bimodal histogram; however, it is susceptible to noise and non-uniform illumination [43]. As Fig. 4 (a) shows, pixel intensities in I_{diff} are spatially dependent with dendrites having higher intensity at the centre as compared with the edges. The subroutine implements column-wise Otsu thresholding, ensuring that the threshold captures as much detail of the columnar front as possible. The threshold's output is a binary image representing the newly formed solid between the two input frames. Fig. 4 (b) shows the resulting binary image with pixels that passed the Otsu threshold shown in white (i.e., with a binary value of 1) and pixels failing the threshold are shown in black (i.e., with a binary value of 0). The algorithm filters white areas in Fig. 4 (b) with less than 2000 connected pixels (8-connected) to remove small defects or spurious features from the threshold. The first pixel in each column of the binary image (Fig. 4 (b)) that passes the threshold defines the location of the contour, $\mathbf{c}_{ij}$, where i indexes over the timesteps of the video sequence and where each timestep has j points, one for each column of the cropped image. Fig. 4 (c) shows the resulting contour overlaid on $I_{c,t+\Delta t}$. The figure includes the local maxima of the contour, which are used for further processing steps.

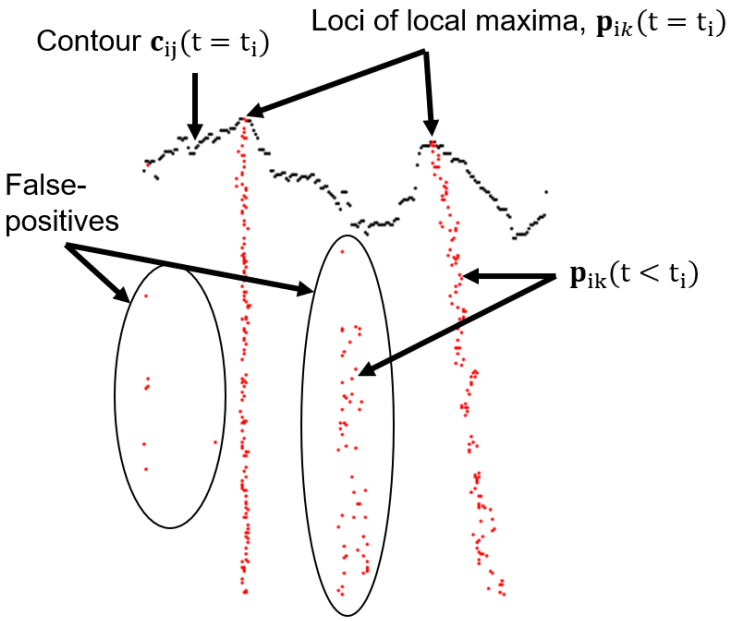

Fig. 5. Close up view of contour (black) and loci of the local maxima from both the current timestep and a selection of previous timesteps (red).

2.3.3 Tip-Data Extraction

Local maxima of the contours at a given timestep can indicate tip positions of columnar dendrites. However, the initial data consists of numerous false positives, and further elimination processing is needed. A subroutine extracts and groups the data in $\mathbf{p}_{ik}$ into separate clusters associated with each columnar dendrite. Since primary columnar dendrites grow uniaxially, the subroutine classifies data points by approximating straight lines through the locus of tip positions of a given primary columnar dendrite. Fig. 5 shows a close up of the contour at a time t_i, and loci of the local maxima, $\mathbf{p}_{ik}$, from the current timestep (in black) and a selection of previous timesteps (in red). Input points, $\mathbf{p}_{ik}$, can consist of over 100 dendrites requiring classification, with up to half of the points being outliers. Classical parameter estimation methods, such as least-squares optimisation, are susceptible to outliers and have insufficient robustness. More robust line-estimation techniques such as the Hough transform or an iterative RANSAC approach were evaluated. However, while both methods were adapted to classify multiple dendrites in $\mathbf{p}_{ik}$, most dendrites were only partially classified, and these methods resulted in significant false-positive groupings. A bespoke subroutine has been developed which block processes subsets of $\mathbf{p}_{ik}$ with a RANSAC-type algorithm. After associating each subset's points with a dendrite (or not, as the case arises), the subroutine merges overlapping groups related to a single dendrite. Similar to RANSAC, the bespoke subroutine uses as small an initial data set as feasible and enlarges this set with consistent data when possible. Outliers are points falling outside an error threshold, d, where d defines the maximum deviation attributable to noise. Here, we set the threshold to approximately one-tenth of the observed primary dendrite arm spacing.

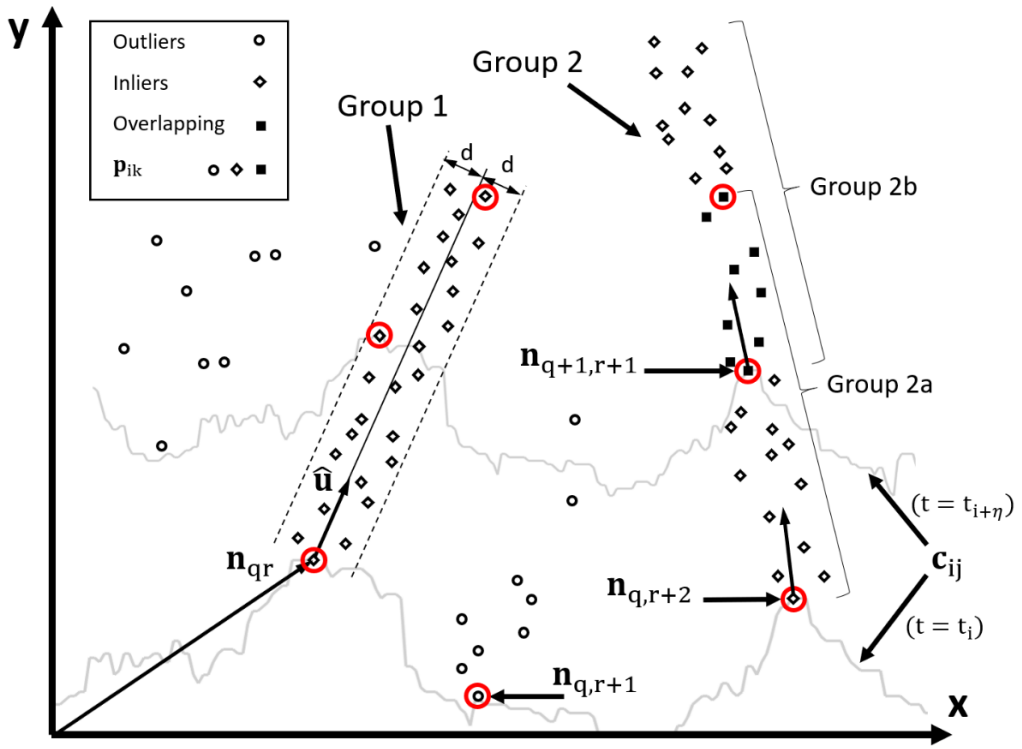

Fig. 6. Schematic illustration of grouping algorithm showing a subsection of $\mathbf{p}_{ik}$ with two contours $\mathbf{c}_{ij}$ and 7 Hypothetical Seed Nodes (HSN's). Group 1 shows a hypothetical linear model with direction vector, $\hat{\mathbf{u}}(\theta)$, hypothetical seed node $\mathbf{n}_{qr}$, and theshold perpendicular distance d for accepting data. θ is optimised to obtain the max number of inliers over the set $\theta \in \mathbb{N}$ [1, 180]. Subgroups 2a and 2b combine into one compund group as $N_{overlap} \geq N$.

The subroutine selects initial nodes from $\mathbf{p}_{ik}$ at intervals separated by η timesteps. These nodes provide a hypothetical starting point from which a group of data may be classified as being associated with a dendrite or not. A sample point is then termed a Hypothetical Seed Node (HSN), and denoted, $\mathbf{n}_{qr}$, (see Fig. 6) where $\mathbf{n}_{qr}$ is the subset $\mathbf{p}_{\eta(i-1)+1,k}$.

For each HSN, the subroutine operates on a subset of points ahead of the node as defined in Eq. (6). The function f_{qrs} in Eq. (4) returns the sum of inliers for a given hypothetical straight-line model. By iterating through θ, the hypothetical model with the largest number of inliers for a given node is obtained. If a threshold number of points fall within the threshold perpendicular distance d from the hypothetical model, the inlier points are then accepted as being associated with a dendrite.

The sum of points within a threshold perpendicular distance, d, to a given theoretical straight-line model and HSN is defined as follows:

$$f_{qrs}(\mathbf{n}_{qr}, \theta_s) = \begin{cases} 1, & \text{if } \left\| (\mathbf{p_{ik}} - \mathbf{n_{qr}}) \times \hat{\mathbf{u}}(\theta_s) \right\| \leq d \\ 0, & \text{otherwise} \end{cases} \quad (4)$$

where $\hat{\mathbf{u}}_s$ is a direction vector for a hypothetical straight-line model given by

$$\hat{\mathbf{u}}_s = \mathrm{Cos}(\theta_s)\mathbf{i} + \mathrm{Sin}(\theta_s)\mathbf{j} \quad (5)$$

The algorithm operates on a subset of points defined relative to the current HSN. Eq. (6) defines indices i and k for the current HSN ($\mathbf{n}_{qr}$) such that all points of $\mathbf{p}_{ik}$ are: (i) within a radial distance, r, from $\mathbf{n}_{qr}$; (ii) have a greater or equal j component, and (iii) exist for all values of t in the interval $t_i \leq t \leq t_{i+2\eta}$

$$i,k \coloneqq \left\{\mathbf{n}_{qr}(t)\middle|\forall(i \wedge k)\left(\left\|\mathbf{p}_{ik}-\mathbf{n}_{\mathbf{qr}}\right\| \leq r\right) \wedge \left(\mathbf{p}_{\mathbf{ik}} \cdot \mathbf{j} \geq \mathbf{n}_{\mathbf{qr}} \cdot \mathbf{j}\right) \wedge (t_i \leq t \leq t_{i+2\eta})\right\} \quad (6)$$

Fig. 6 shows seven HSNs (circled in red) and illustrates the subsets of data for the hypothetical nodes $\mathbf{n}_{qr}$, $\mathbf{n}_{q+1,r}$, $\mathbf{n}_{q,r+1}$, $\mathbf{n}_{q+1,r+1}$, and $\mathbf{n}_{q+1,r+2}$ which, in combination with $\hat{\mathbf{u}}$**,** define the hypothetical straight-line models. HSNs occur at every η timesteps, while (subject to Eq. (6)) subsets of $\mathbf{p}_{ik}$ associated with a given HSN spans 2η timesteps providing an overlap between groups. The subroutine crosschecks the accepted data from time-adjacent groups for overlap, thus providing a criterion for merging the groups. Fig. 6 shows merging of two subgroups, 2a and 2b, where a threshold number of points overlap. Dendrite clusters consisting of 50 points or less are omitted from further processing steps. Position data clusters are sorted according to time, smoothed with a second-order Savitsky-Golay filter with a 50-point window, and linear interpolation of x and y with respect to time is used to fill any missing data points. Finally, dendrite orientation, α, is obtained by orthogonal least squares regression of the x and y coordinates for a given dendrite cluster, while the magnitude of the dendrite tip velocity is determined by

$$v_{i+2} = \frac{\|\mathbf{p}(t_{i+4})-\mathbf{p}(t_i)\|}{t_{i+4}-t_i} \quad (7)$$

In summary, the grouping process works as follows:

(i) Select a seed node, **n**, at time t_i

(ii) Select a subset of points in $\mathbf{p}_{ik}$ near the seed node, i.e., points within a radial distance r from $\mathbf{n}$, with **j** components greater than or equal to that of $\mathbf{n}$, and over a time interval $t_i \leq t \leq t_{i+2m}$

(iii) Maximise $f(\mathbf{n}_{qr}, \theta_s)$ by iterating through $\theta, \forall\theta \in \mathbb{N}[1,180]$.

(iv) Check time-adjacent groups for the merging criterion.

The pre-processing, contouring and tip-data extraction algorithm allows tips to be tracked with their velocity and orientation being measured. Growth vectors are applied to the moving tips within the video data on a frame-by-frame basis, as shown in the supplementary material. These videos give a clear visual reference for the growth rate of each identified dendrite tip. Given that a stationary thermocouple was inserted inside the crucible (and within the observation window) to measure the melt temperature, it was possible to observe the moment that the tips crossed over the

thermocouple. Hence, this feature facilitated the instantaneous tip temperature measurement as the solidification front crossed the thermocouple.

2.4 Theoretical models

The Lipton-Glicksman-Kurz model of dendrite growth is based on the Ivantsov formulation for the solute field around a parabolic dendrite tip. Taking into account the diffusion field around a dendrite tip, the dimensionless supersaturation, $\Omega = \frac{C^* - C_0}{C^*(1-k_0)}$, is defined as:

$$\Omega = \mathrm{Pexp(P)E_1(P)} \equiv \mathrm{Iv(P)} \tag{8}$$

where P is the solutal Péclet number given as P=VR/2D, and E_1 is the exponential integral function. A solution to this equation requires a stability criterion which is given by

$$R = \left\{\frac{\Gamma}{\sigma^*(mG_C - G)}\right\}^{\frac{1}{2}} \tag{9}$$

where Γ is the Gibbs-Thompson coefficient representing surface energy, σ^* is the stability parameter and m is the liquidus slope. G_C is the solutal gradient in the liquid at the tip interface and is given as

$$G_C = -\frac{2P\,C^*(1-k_0)}{R} \tag{10}$$

where C^* is the composition in the liquid at the tip interface, k_0 is the equilibrium partition coefficient and R is the dendrite tip radius. Table 2 lists the alloy's thermophysical properties. The LGK model requires an iterative solution to the preceding set of equations, and the undercooling at the tip is taken as the sum of the solutal and curvature undercooling terms. The stability parameter, σ^*, determines the operating point for the dendrite tip. Originally, the LGK model used a general parameter of $1/4\pi^2$ = 0.025; however, experimental evidence is needed to determine the alloy system's actual parameter in question [44]. Sturz and Zimmermann [11] determined the stability parameter for NPG-37.5wt.%DC by fitting the LGK model to microgravity data. New information has come to light on the diffusivity of D-Camphor in NPG [37] (with $D_L = 9.7 \times 10^{-11} m^2/s$). Applying the same fitting exercise as Sturz and Zimmermann but with the updated diffusivity gives a stability parameter of $\sigma^* = 4.15 \times 10^{-3}$.

To account for the effect of fluid flow around a dendrite tip, Cantor and Vogel [28] proposed the existence of a diffusional boundary layer of finite length, δ, around the tip. The approach of assuming a finite boundary later is comprehensively reviewed by McFadden and Browne [32], and

adaptation to the LGK model is the new term in the dimensionless supersaturation equation that accounts for the boundary layer thickness as follows:

$$\Omega = \mathrm{P}\exp(\mathrm{P})\left[\mathrm{E}_1(\mathrm{P}) - \mathrm{E}_1\left(\mathrm{P}\left(1+\frac{2\delta}{\mathrm{R}}\right)\right)\right] \tag{11}$$

Hence, with Cantor and Vogel's solution to the dimensionless supersaturation equation, different boundary layer thickness values can be assumed a priori and included in the version of the LGK model adapted for fluid flow (LGK-CV).

3 Results

Six directional solidification test scenarios are presented using a transparent alloy NPG-35wt.%DC. The apparatus facilitated directional solidification with a controlled temperature gradient, cooling rate and equilibrium liquidus isotherm speed (for a more detailed description of the apparatus, see [10]). Table 1 lists the thermal processing parameters for all six experiments covering a range of isotherm speeds between 1.13 and 4.53 $\mu m/s$. In-situ microscopic video sequences of all six test cases were processed with the newly developed computer vision algorithm. To appreciate the advantage of an automatic detection system, a total of 385 columnar dendrite tips were tracked over all six tests. Table 3 summarises the processed results for each test, including the total number of tips tracked ($\mathrm{N_{total}}$), the number of tips crossing the internal thermocouple ($\mathrm{N_{crossing}}$), the mean tip velocity ($\overline{\mathrm{v}}_\mathrm{t}$), the mean undercooling ($\Delta\overline{\mathrm{T}}$) for tips that crossed the internal thermocouple, and their standard uncertainties ($\mathrm{u}_{\overline{\mathrm{v}}_\mathrm{t}}$ and $\mathrm{u}_{\Delta\overline{\mathrm{T}}}$).

Table 3. Summary of columnar dendrite tips tracked during each test detailing the average tip velocities and undercoolings, and their associated standard uncertainties.

Test no.	$\mathrm{N_{total}}$	$\mathrm{N_{crossing}}$	$\overline{\mathrm{v}}_\mathrm{t}$	$\mathrm{u}_{\overline{\mathrm{v}}_\mathrm{t}}$	$\Delta\overline{\mathrm{T}}$	$\mathrm{u}_{\Delta\overline{\mathrm{T}}}$
	#	#	$\mu m/s$	$\mu m/s$	K	K
I	47	6	1.18	0.03	0.95	0.04
II	56	21	2.38	0.02	2.29	0.02
III	42	11	3.62	0.09	2.95	0.05
IV	62	14	1.98	0.03	3.43	0.07
V	97	27	3.54	0.05	5.61	0.03
VI	81	16	5.40	0.14	5.53	0.05

As mentioned, the NPG-DC hypoeutectic alloy has been in microgravity investigations to study columnar growth structures and columnar to equiaxed transitions [11]. Fig. 8 shows results of dendrite tip velocity and undercooling from the present work from a total of 95 dendrite tips crossing the internal thermocouple. Tests numbers from I to III are shown with triangle, circle, and square markers with white marker face colour, while test numbers IV to VI are shown with triangle, circle, and square markers with grey marker face colours. Fig. 8 also compares the present work with the TRACE experiment conducted in microgravity with otherwise similar processing parameters (NPG-37.5wt.%DC and G = 16.5 K/cm). Solidification studies on sounding rocket missions are typically

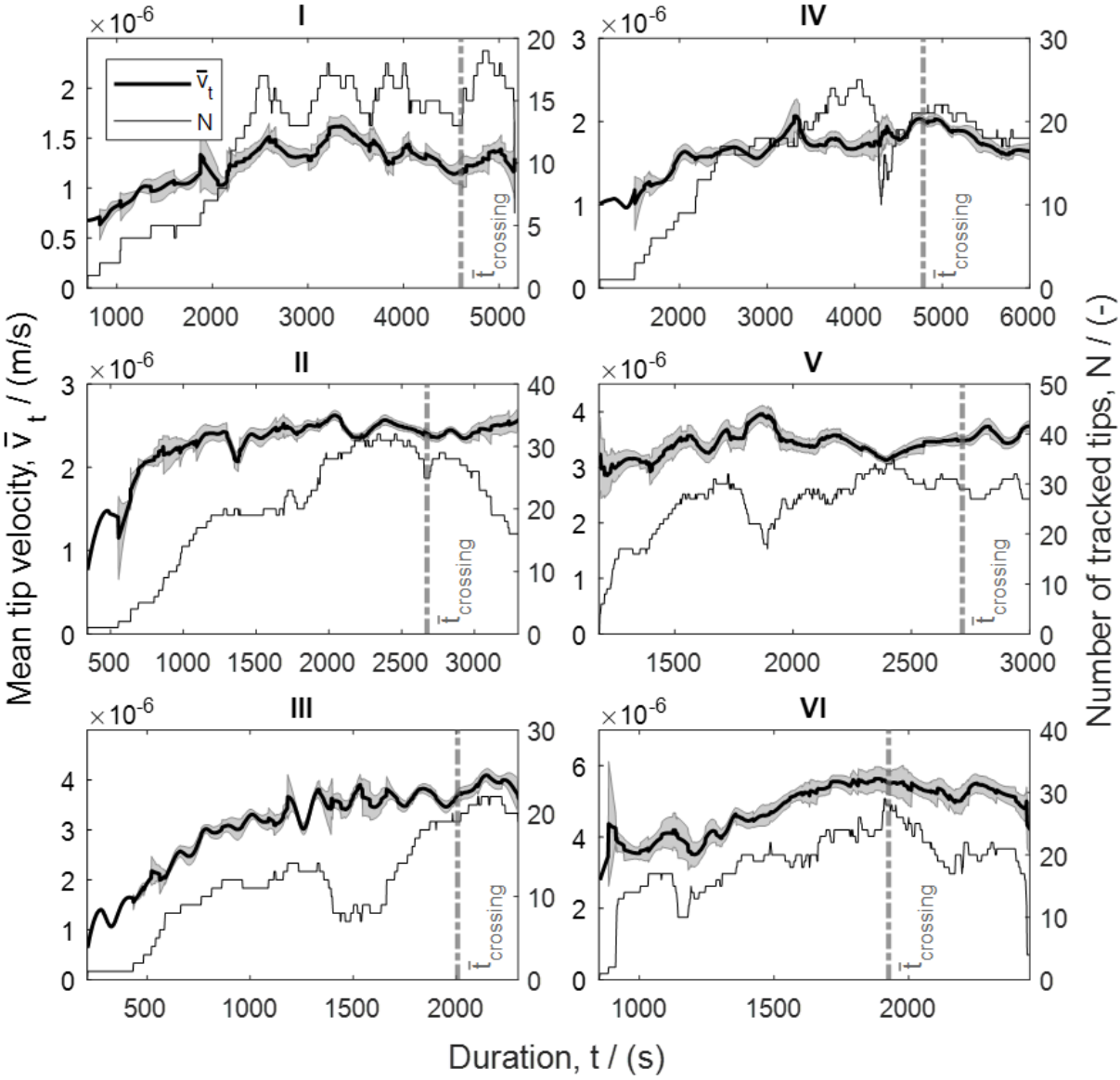

Fig. 7. Mean dendrite tip velocity, $\bar{v}_t$, and number of tips, N, tracked versus time for tests I to VI. The graphs show mean velocities with two standard errors applied over the interval, The vertical dashed lines indicating average time, $t_{crossing}$, when dendrite tips crossed the internal thermocouple.

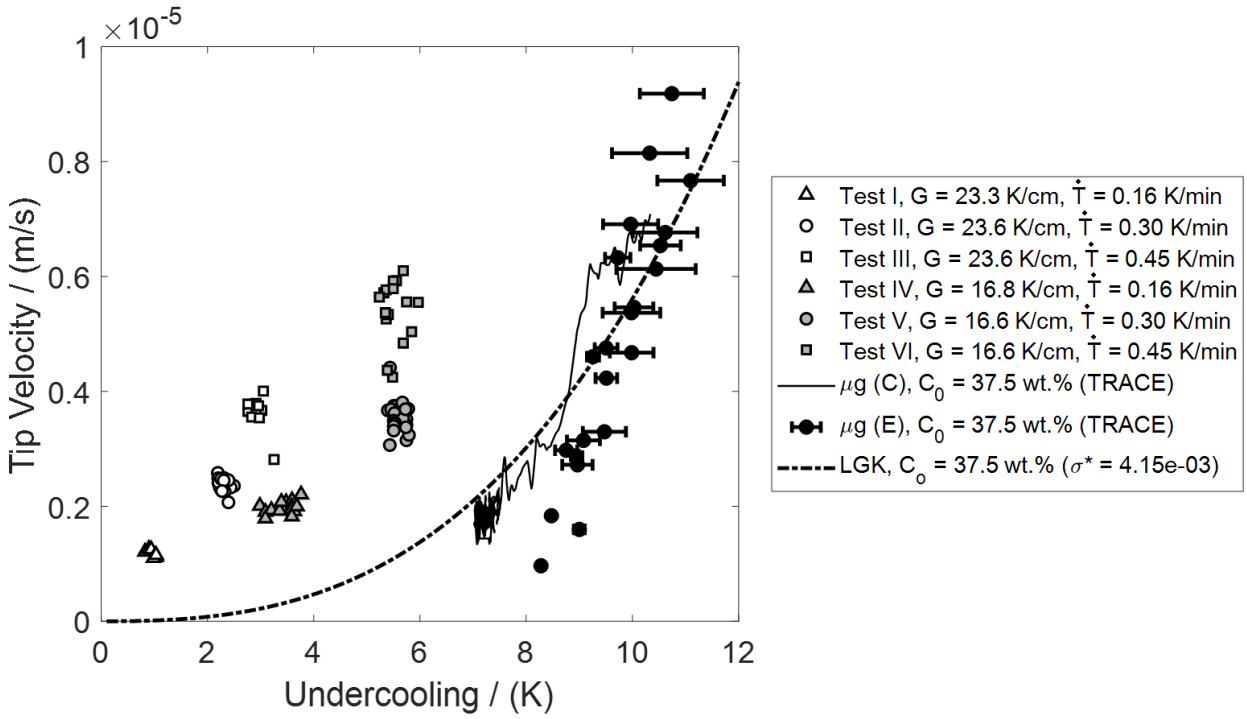

Fig. 8. Dendrite tip velocity versus undercooling for the present work (Test cases I – VI, C_o = 35wt.%, shown with symbols △○□△○□, respectively) compared with measurements from the TRACE microgravity experiment (C_o = 37.5wt.%)(C- columnar, E - equiaxed.) and the LGK growth law.

performed under transient conditions and higher undercooling to allow appreciable growth during the 4-5 minute microgravity window. Due to relaxed time constraints in terrestrial experimentation, the current test cases cover the low undercooling range to fill this knowledge gap. In addition to the experimental data, Fig. 8 shows the results of the Lipton Glicksman-Kurz (LGK) dendrite model but with the stability parameter, σ*, adjusted after a data-fitting exercise. As described in the methodology section, the LGK model, which is derived on a solutal diffusion basis, is fitted to the microgravity datasets.

Fig. 7 shows the mean dendrite tip velocity, $\bar{v}_t \pm k u_{\bar{v}_t}$. The experimental standard deviation of the mean, $u_{\bar{v}_t}$, is defined by

$$u_{\bar{v}_t} = \sqrt{\frac{1}{N(N-1)} \sum_{i=1}^{N} (\bar{v}_t - v_i)^2} \tag{12}$$

and is determined for N dendrite tips tracked at a given time. Expanded uncertainty intervals are provided with a coverage factor of k=2 and hence 95% confidence interval. Fig. 7 shows the progression of the number of tips tracked, N, over time for the six tests. A vertical dashed line indicates the mean time, $\bar{t}_{crossing}$, that dendrite tips crossed the internal thermocouple.

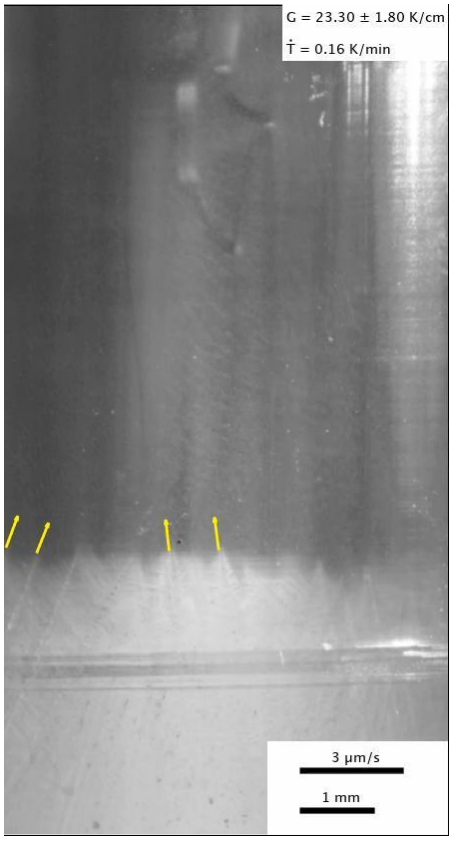

Video 1 Augmented video data for test 1

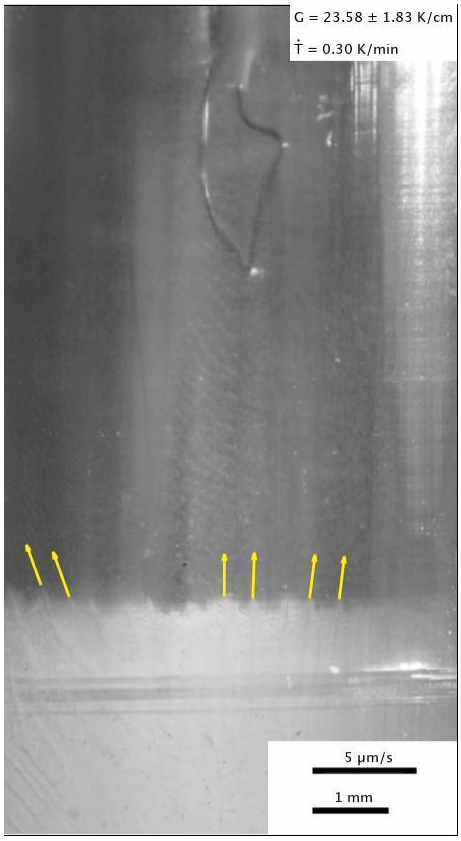

Video 2 Augmented video data for test 2

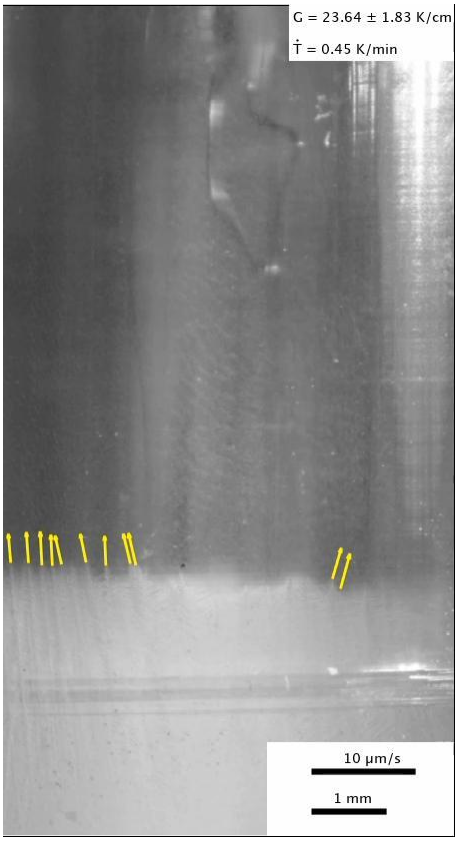

.**Video 3** Augmented video data for test 3

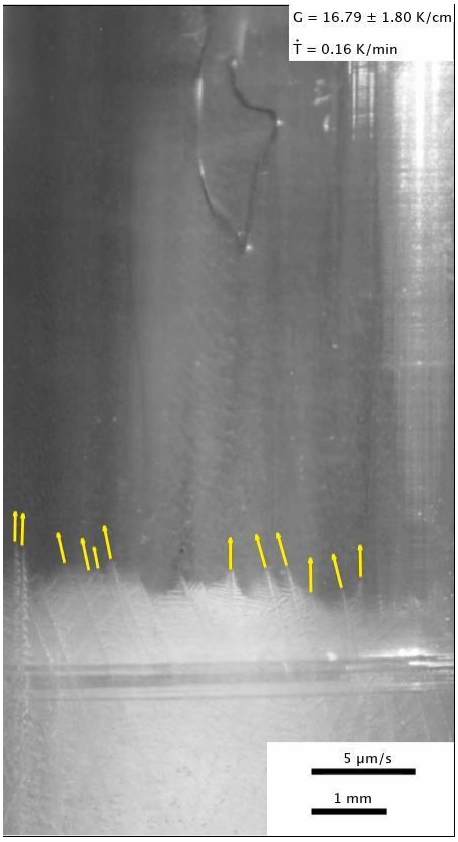

Video 4 Augmented video data for test 4

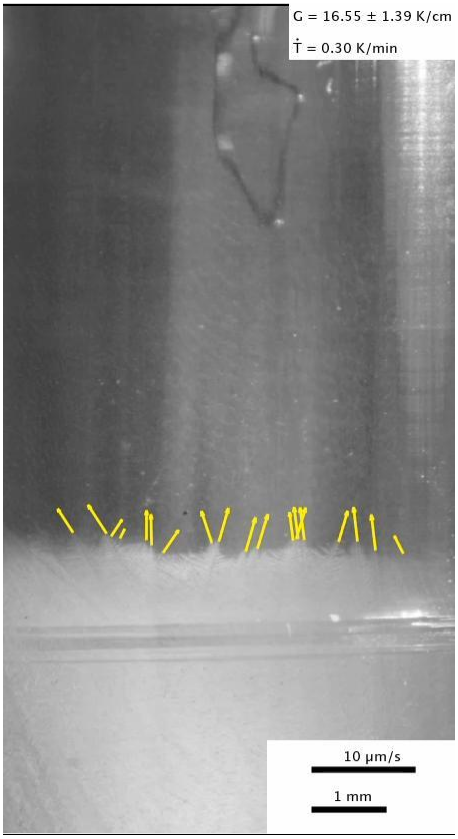

Video 5 Augmented video data for test 3

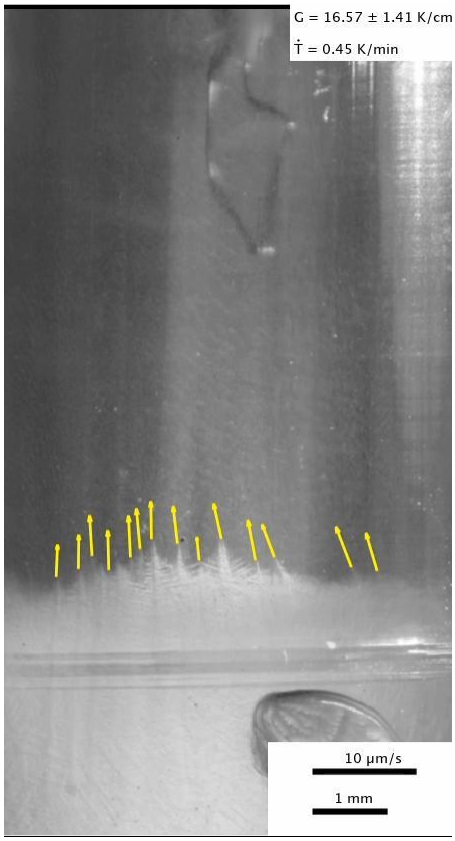

Video 6 Augmented video data for test 3

4 Discussion

Results are presented using a new computer vision algorithm giving the growth rates and undercooling levels of multiple columnar dendrite tips during directional solidification of bulk transparent alloy NPG-35wt.%DC. Six directional solidification tests were conducted with a controlled temperature gradient, cooling rate, and hence isotherm speed. The computer vision algorithm tracked a total of 385 columnar dendrite tips. In the following section, key points are discussed: (i) the performance and general results of the computer vision algorithm, (ii) the comparison of current tip velocity and undercooling data to relevant microgravity data, and (iii) and the comparison of experimental data to theoretical LGK and modified LGK models of dendrite tip velocity.

Fig. 7 provides a summary overview of all the dendrite tip tracking data with mean dendrite tip velocity, $\bar{v}_t$ ($\pm$2SEM) and the total number of tips tracked, N, at any given time, t. Generally, the tip tracking shows an initial transient phase, with $\bar{v}_t$ tending to increase until quasi-steady growth conditions are attained with $\bar{v}_t$ becoming approximately fixed. Fig. 8 shows the instantaneous dendrite tip velocity and associated undercooling measured at the moment when the dendrite tips crossed the internal thermocouple, T_i. Fig. 7 shows the average time that dendrite tips crossed the internal thermocouple, $t_{crossing}$. In all cases, dendrite tip and undercooling measurements were captured during the quasi-steady growth phase. The numbers of dendrite tips involved at the thermocouple crossing stage in all cases are within the range from 6 to 27 tips. Hence, reasonable statistical information is expected.

Velocity vectors in the in-situ video data (refer to the supplementary materials) show oscillations of individual dendrite tip velocities; in some cases, there is an interplay between neighbouring dendrite

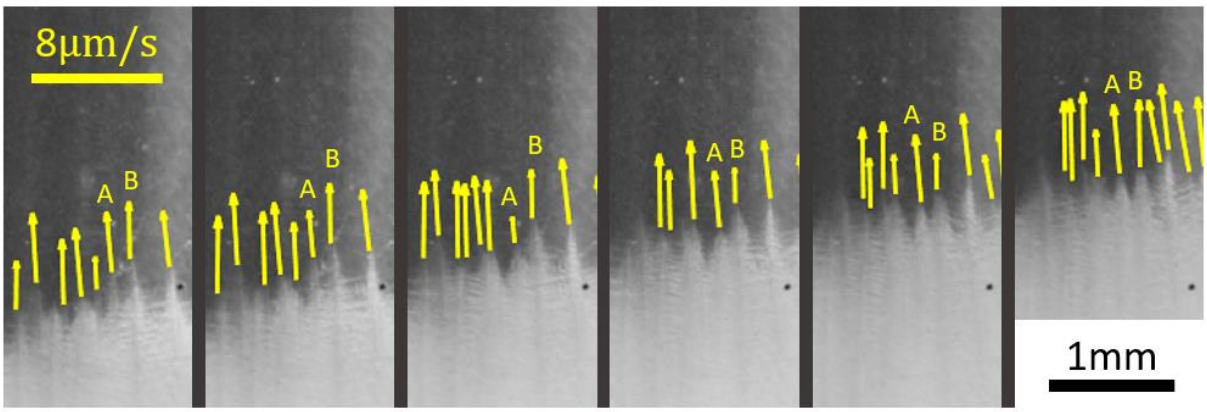

Fig. 9. Image sequence from test VI shows competitive interplay between two neighboruing dendrites. Tip A slows down falling behind tip B, then B slows down and A speeds up until they are side by side.

tips where one races out ahead, and then the other catches up. In general, the fluctuations in dendrite tip velocity are out of phase. Fig. 9 clearly shows the interplay between adjacent columnar dendrites (annotated A and B). Initially, dendrite A fell behind (frames 2 - 3) then increased in growth rate (frame 4) while B simultaneously slowed down (frames 4 – 5), allowing dendrite A to catch up to dendrite B. Since there is an imposed temperature gradient, upwards solidification is usually deemed thermally stable. This is because density typically decreases with temperature, and temperature increases in the vertical direction. The effect of gravity on a fluid with its highest density liquid at the solid-liquid interface suppresses thermal convection ahead of the front. The out-of-phase growth oscillation between dendrites is likely due to the solutal interaction and alternating changes in the composition gradient in liquid, G_c, ahead of the tips. The solute, D-camphor, is less dense than NPG, so the partitioning (rejection) of solute into the liquid causes the density to be lower ahead of the tips and this leads to convection due to solutal instability. Hence, the solidification is thermally stable but solutally unstable, and this could lead to fluctuations in the solute field ahead of the dendrite tips. It has been shown elsewhere [45] that unsteady or oscillatory growth can occur because of changes in the solute field ahead of the dendrite even though thermal conditions are stable. Even though evidence shows that the dendrite growth has periods of acceleration followed by deceleration, the net effect is growth at the average rate as given by $\bar{v}_t$. Since the solutal diffusion length (17.4 μm), is much less than the distance between dendrites A and B (approx. 145 um based on measurement in ImageJ), the interaction which resulted in a significant variation in dendrite tip velocity, was most likely related to thermosolutal flow.

However, Fig. 7 III shows periodic variations in the mean tip velocity in excess of the measurement uncertainty. The periodicity in $\bar{v}_t$ is evidence of competitive growth between neighbouring dendrites; impingement of the faster misaligned tips which are subsequently not being tracked and thus decrease $\bar{v}_t$. Dendrite tip velocity may decrease on the scale of the solidification front due to solute piling at the dendrite tips. Subsequent thermosolutal convection may replace the solute enriched liquid with a lower composition liquid causing dendrite tip velocity to accelerate again. In test III, the effect could be occurring across the scale of the solidification front, thus affecting the mean tip velocity.

Fig. 8 compares terrestrial work on binary alloy NPG-35wt.%DC with similar microgravity data from the TRACE campaign by Sturz et al. [11]. Three out of the six tests presented in this manuscript (see Table 1 for test no. IV-VI) were conducted at a temperature gradient of 16.5 – 16.8 K/cm, thus providing the best comparison to TRACE (16.5 K/cm with 37.5wt.% composition). Fig. 8 shows a notable difference in tip velocity and undercooling relationship for the terrestrial case as compared with TRACE. Dendrite tip undercooling in the diffusive microgravity conditions were between 1.48 and 2.42 times that of terrestrial conditions for the same tip velocity (datapoints within 0.05 μm/s). As mentioned, the solidification conditions are expected to be thermally stable but solutally unstable, i.e. the solute partitioned at the solid-liquid interface is lower density than the bulk liquid, and therefore more buoyant. Hence, even with the positive vertical temperature gradient, convective instabilities can occur even if the liquid's net density decreases with height. The significant difference between the results in this study and TRACE is attributed to buoyancy-driven thermosolutal convection. Glicksman et al. showed similar findings for free dendritic growth in microgravity and terrestrial conditions with the transparent alloy succinonitrile [26,27]; the authors reported that tip velocity increased by a factor of two at lower undercooling and that the LGK diffusion solution to the dendrite problem was not consistent with the terrestrial experimental data. Additionally, Cantor and Vogel's theoretical modelling indicates that the effect of fluid flow on tip velocity undercooling relationship is more significant for a constitutional dendrite versus a thermal

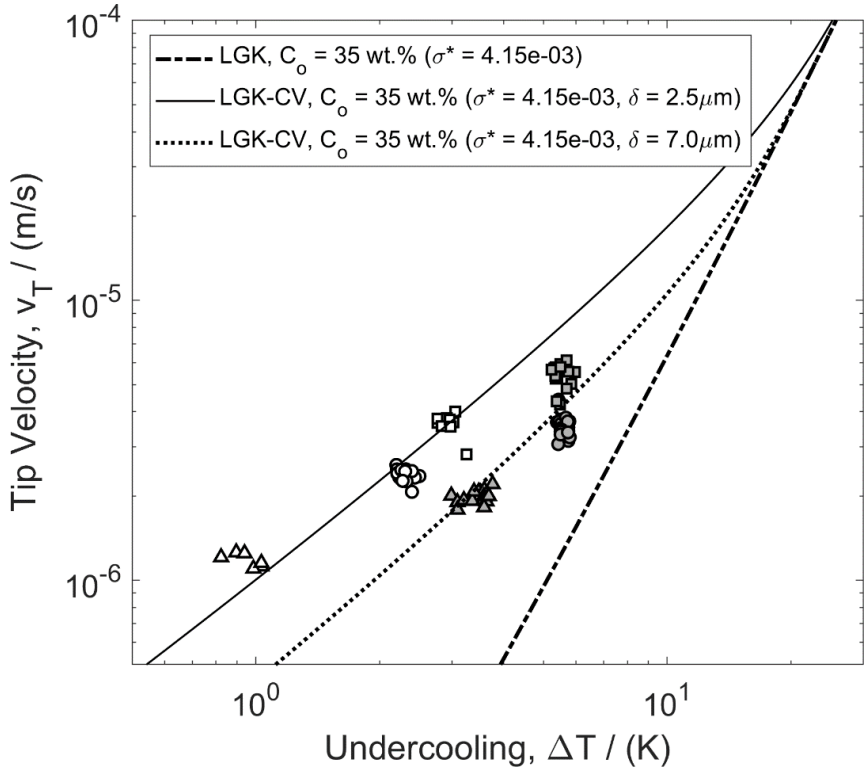

Fig. 10. Experimental results with comparisons to the LGK model and LGK model adapted with the solution of Cantor and Vogel (LGK-CV) at two values of δ: 2.5 μm and 7.0 μm. White markers represent data at approx 23 K/cm; grey markers at approx. 16 K/cm

dendrite.

Several models have been developed to account for the effect of thermosolutal flow on dendrite tip velocity. The modified LGK model, which assumes diffusive transport inside a boundary layer of length δ and infinite mixing outside the boundary layer, was applied with finite boundaries of thickness 2.5 and 7 μm. Fig. 10 shows the LGK model based on $\mathrm{D_L} = 9.7 \times 10^{-11}\mathrm{m^2/s}$, $\mathrm{C_0} = 35$, and $\sigma^* = 4.15 \times 10^{-3}$, which is representative of microgravity or diffusional conditions. The two corresponding fits with the modified-LGK show good agreement with the terrestrial experimental data where thermosolutal convection is assumed. For comparison purposes, the diffusional solutal lengths with no convection present (given as $l_s=D_l/v_t$) in the range of 1.0 to 6.0 μm/s growth rate would give purely diffusional solute boundaries of between 17 – 98 μm. Since the approximated boundary thickness of 2.5 and 7 μm are smaller than those expected for the pure diffusion case, we can expect the corresponding composition gradients at the tip interface to be greater in magnitude owing to the thermosolutal convection; hence, growth velocities are higher than predicted by the LGK growth law.

5 Conclusion

A bespoke solidification apparatus and a new experimental procedure has been developed that uses a novel computer vision algorithm to automatically track the position and velocity of multiple columnar dendrites during in-situ observation. In this study, the computer vision algorithm was used to track a total of 385 dendrite tips. A total of 95 dendrite tips were observed to cross an internal thermocouple in the melt; hence, instantaneous measurement of tip velocity and undercooling was provided. The results have been compared with similar microgravity experimental results, and a marked difference is reported between the terrestrial and microgravity data. Comparison was made to the classical LGK growth law based on solute diffusion without convection. At the same growth rates, terrestrial undercoolings were between 0.41 and 0.68 times the predicted growth rates. However, when modifications were made to the theoretical LGK to compensate for the effect of convection, results gave good agreement for finite boundary layers of lengths in the range 2.5 to 7.0 μm.

Other effects that were observed and attributed to convection were oscillations of the growth rate (i.e., acceleration-deceleration cycles). Nevertheless, even with undulations of the growth rate, the observed net effect in all cases was growth at an average velocity under thermally steady conditions.

The new computer vision algorithm was demonstrated to be highly beneficial since, with 385 dendrite tip tracked, it provides statistical and quantitative data otherwise too laborious to capture manually. In addition to the scaling up of quantitative data analysis, the visual results from the algorithm enhanced the ability to make qualitative observations. For example, velocity vectors shown in videos for test no. V and VI illustrate the classic Walton-Chalmers predicted behaviour [46], i.e. misaligned dendrites lag the aligned dendrites and have a y-component of velocity close to that of the aligned dendrites. Further work with the computer vision algorithm may provide deeper insights into competitive growth and the Walton-Chalmers model. The results from this study and the application of this new procedure to other scenarios will be of interest to the modelling community who are interested in modelling competitive columnar growth, for example, the work of [47–52].

Acknowledgements

This work was supported by the European Space Agency (ESA) [contract number 4200014313NL/SH, CCN009 to AO-99-117] and by ESA PRODEX [contract number 4000110385 CN 3] as part of the CETSOL Microgravity Application Programme. ESA PRODEX funding is managed by the Irish Space Delegation at Enterprise Ireland. We wish to acknowledge Laszlo Sturz and Gerhard Zimmermann for sharing TRACE experimental data and for fruitful conversations.

Data Availability

The raw and processed data required to reproduce these findings are available to download from:

https://data.mendeley.com/datasets/2tb6nmc3jg/draft?a=4e9ac197-db23-4336-9deb-705a79f380c3.

References

[1] W. Kurz, M. Rappaz, R. Trivedi, Progress in modelling solidification microstructures in metals and alloys. Part II: dendrites from 2001 to 2018, Int. Mater. Rev. 66 (2021) 30–76. https://doi.org/10.1080/09506608.2020.1757894.

[2] D.J. Browne, F. García-Moreno, H. Nguyen-Thi, G. Zimmermann, F. Kargl, R.H. Mathiesen, A. Griesche, O. Minster, Overview of In Situ X-ray Studies of Light Alloy Solidification in Microgravity, J. Miner. Met. Mater. Soc. (2017) 581–590. https://doi.org/10.1007/978-3-319-52392-7_80.

[3] M. Asta, C. Beckermann, A. Karma, W. Kurz, R. Napolitano, M. Plapp, G. Purdy, M. Rappaz, R. Trivedi, Solidification microstructures and solid-state parallels: Recent developments, future directions, Acta Mater. 57 (2009) 941–971. https://doi.org/10.1016/j.actamat.2008.10.020.

[4] W. Huang, L. Wang, Solidification researches using transparent model materials - A review, Sci. China Technol. Sci. 55 (2012) 377–386. https://doi.org/10.1007/s11431-011-4689-1.

[5] H. Nguyen-thi, In situ observation of solidification patterns in diffusive conditions, Acta Mater. 108 (2016) 325–346. https://doi.org/10.1016/j.actamat.2016.01.024.

[6] E. Liotti, C. Arteta, A. Zisserman, A. Lui, V. Lempitsky, P.S. Grant, Crystal nucleation in metallic alloys using x-ray radiography and machine learning, Sci. Adv. 4 (2018) 1–9. https://doi.org/10.1126/sciadv.aar4004.

[7] A. Baskaran, G. Kane, K. Biggs, R. Hull, D. Lewis, Adaptive characterization of microstructure dataset using a two stage machine learning approach, Comput. Mater. Sci. 177 (2020) 109593. https://doi.org/10.1016/j.commatsci.2020.109593.

[8] S. McFadden, R.P. Mooney, L. Sturz, G. Zimmermann, A Nucleation Progenitor Function approach to polycrystalline equiaxed solidification modelling with application to a microgravity transparent alloy experiment observed in-situ, Acta Mater. 148 (2018) 289–299. https://doi.org/10.1016/j.actamat.2018.02.012.

[9] A.G. Murphy, W.U. Mirihanage, D.J. Browne, R.H. Mathiesen, Equiaxed dendritic solidification and grain refiner potency characterised through in situ X-radiography, Acta Mater. 95 (2015) 83–89. https://doi.org/10.1016/j.actamat.2015.04.060.

[10] T. Hughes, S. McFadden, A.J. Robinson, A front-tracking measurement technique for in-situ columnar and equiaxed structure growth with controlled solidification, Meas. Sci. Technol. 32 (2020) 045903. https://doi.org/10.1088/1361-6501/abcb24.

[11] L. Sturz, G. Zimmermann, In-situ and real-time investigation of the columnar-equiaxed transition in the transparent alloy system neopentylglycol-camphor onboard the sounding rocket TEXUS-47, J. Phys. Conf. Ser. 327 (2011) 1–9. https://doi.org/10.1088/1742-6596/327/1/012002.

[12] G. Zimmermann, M. Hamacher, L. Sturz, Effect of zero, normal and hyper-gravity on columnar dendritic solidification and the columnar-to-equiaxed transition in Neopentylglycol-(D)Camphor alloy, J. Cryst. Growth. 512 (2019) 47–60. https://doi.org/10.1016/J.JCRYSGRO.2019.01.043.

[13] A. Buffet, H. Nguyen Thi, A. Bogno, T. Schenk, N. Mangelinck-Noël, G. Reinhart, N. Bergeon, B. Billia, J. Baruchel, Measurement of solute profiles by means of synchrotron X-ray radiography during directional solidification of Al - 4 wt% Cu alloys, Mater. Sci. Forum. 649 (2010) 331–336. https://doi.org/10.4028/www.scientific.net/MSF.649.331.

[14] A. Bogno, H. Nguyen-Thi, A. Buffet, G. Reinhart, B. Billia, N. Mangelinck-Noël, N. Bergeon, J. Baruchel, T. Schenk, Analysis by synchrotron X-ray radiography of convection effects on the dynamic evolution of the solid-liquid interface and on solute distribution during the initial transient of solidification, Acta Mater. 59 (2011) 4356–4365. https://doi.org/10.1016/j.actamat.2011.03.059.

[15] D. Ruvalcaba, R.H. Mathiesen, D.G. Eskin, L. Arnberg, L. Katgerman, In situ observations of dendritic fragmentation due to local solute-enrichment during directional solidification of an aluminum alloy, Acta Mater. 55 (2007) 4287–4292. https://doi.org/10.1016/j.actamat.2007.03.030.

[16] M. Becker, S. Klein, F. Kargl, In-situ solute measurements with a laboratory polychromatic microfocus X-ray source during equiaxed solidification of an Al-Ge alloy, Scr. Mater. 124 (2016) 34–37. https://doi.org/10.1016/j.scriptamat.2016.06.032.

[17] J. Mihailovic, C. Beckermann, Development of a two-dimensional liquid species concentration measurement technique based on absorptiometry, Exp. Therm. Fluid Sci. 10 (1995) 113–123. https://doi.org/10.1016/0894-1777(94)00069-K.

[18] B. Nenchev, J. Strickland, K. Tassenberg, S. Perry, S. Gill, H. Dong, Automatic recognition of dendritic solidification structures: DenMap, J. Imaging. 6 (2020) 1–12. https://doi.org/10.3390/jimaging6040019.

[19] J. Miller, M. Strangwood, S. Steinbach, N. Warnken, Skeletonisation to Find the Centre of Dendrites Traced from a 2D Microstructural Image, Proc. 5th Decenn. Int. Conf. Solidif. Process. (2017) 2–5. https://elib.dlr.de/114081/.

[20] F.L. Mota, K. Ji, T. Lyons, L.L. Strutzenberg, R. Trivedi, A. Karma, N. Bergeon, In situ observation of growth dynamics in DECLIC Directional Solidification Insert onboard ISS: DSI-R flight campaign, in: Proc. 70th Int. Astronaut. Congr., Washington, United States, 2019. https://hal.archives-ouvertes.fr/hal-02336173.

[21] G.P. Ivantsov, The temperature field around a spherical, cylindrical, or pointed crystal growing in a cooling solution, in: Dokl. Akad. Nauk SSSR, 1947: pp. 567–569.

[22] G.P. Ivantsov, Temperature field around a spherical, cylindrical, and needle-shaped crystal, growing in a pre-cooled melt, 1985. https://ntrs.nasa.gov/api/citations/19850023698/downloads/19850023698.pdf.

[23] J. Lipton, M.E. Glicksman, W. Kurz, Dendritic growth into undercooled alloy metals, Mater. Sci. Eng. 65 (1984) 57–63. https://doi.org/10.1016/0025-5416(84)90199-X.

[24] J.S. Langer, J. Müller-Krumbhaar, Stability effects in dendritic crystal growth, J. Cryst. Growth. 42 (1977) 11–14. https://doi.org/10.1016/0022-0248(77)90171-3.

[25] M.E. Glicksman, M.B. Koss, E.A. Winsa, Dendritic Growth Velocities in Microgravity, Phys. Rev. Lett. 73 (1994) 573–576. https://doi.org/10.1103/PhysRevLett.73.573.

[26] M.E. Glicksman, M.B. Koss, L.T. Bushnell, J.C. Lacombe, E.A. Winsa, Dendritic Growth of Succinonitrile in Terrestrial and Micro gravity Conditions as a Test of Theory, ISIJ Int. 35 (1995) 604–610. https://doi.org/10.2355/isijinternational.35.604.

[27] L.A. Tennenhouse, M.B. Koss, J.C. LaCombe, M.E. Glicksman, Use of microgravity to interpret dendritic growth kinetics at small supercoolings, J. Cryst. Growth. 174 (1997) 82–89. https://doi.org/10.1016/S0022-0248(96)01064-0.

[28] B. Cantor, A. Vogel, Dendritic solidification and fluid flow, J. Cryst. Growth. 41 (1977) 109–123. https://doi.org/10.1016/0022-0248(77)90104-X.

[29] R. Ananth, W.N. Gill, Self-consistent theory of dendritic growth with convection, J. Cryst. Growth. 108 (1991) 173–189. https://doi.org/10.1016/0022-0248(91)90365-C.

[30] D. Canright, S.H. Davis, Buoyancy effects of a growing, isolated dendrite, J. Cryst. Growth. 114 (1991) 153–185. https://doi.org/10.1016/0022-0248(91)90690-7.

[31] Q. Li, C. Beckermann, Modeling of free dendritic growth of succinonitrile-acetone alloys with thermosolutal melt convection, J. Cryst. Growth. 236 (2002) 482–498. https://doi.org/10.1016/S0022-0248(01)02390-9.

[32] S. McFadden, D.J. Browne, A generalised version of an Ivantsov-based dendrite growth model incorporating a facility for solute measurement ahead of the tip, Comput. Mater. Sci. 55 (2012) 245–254. https://doi.org/10.1016/j.commatsci.2011.12.011.

[33] C.A. Gandin, G. Guillemot, B. Appolaire, N.T. Niane, Boundary layer correlation for dendrite tip growth with fluid flow, Mater. Sci. Eng. A. 342 (2003) 44–50. https://doi.org/10.1016/S0921-5093(02)00261-7.

[34] M.E. Glicksman, S.R. Coriell, G.B. McFadden, Interaction of flows with the crystal-melt interface, Ann. Rev. Fluid Mech. 18 (1986) 307–333. https://doi.org/10.1146/annurev.fl.18.010186.001515.

[35] L. Sturz, M. Hamacher, G. Zimmermann, In-situ observation of equiaxed dendritic growth and interaction in microgravity, in: Z. Fan (Ed.), 6th Decenn. Int. Conf. Solidif. Process., Brunel University London Press, Old Windsor, 2017: pp. 300–303.

[36] V.T. Witusiewicz, L. Sturz, U. Hecht, S. Rex, Thermodynamic description and unidirectional solidification of eutectic organic alloys: II. (CH3)2C(CH2OH)2-(NH2)(CH3)C(CH2OH)2system, Acta Mater. 52 (2004) 5071–5081. https://doi.org/10.1016/j.actamat.2004.07.013.

[37] V.T. Witusiewicz, L. Sturz, U. Hecht, S. Rex, Lamellar coupled growth in the neopentylglycol-(D)camphor eutectic, J. Cryst. Growth. 386 (2014) 69–75. https://doi.org/10.1016/j.jcrysgro.2013.09.035.

[38] U. Bayram, S. Aksöz, N. Maraşl, Solidliquid interfacial energy of neopentylglycol solid solution in equilibrium with neopentylglycol(D) camphor eutectic liquid, J. Cryst. Growth. 338 (2012) 181–188. https://doi.org/10.1016/j.jcrysgro.2011.11.005.

[39] Ü. Bayram, S. Aksöz, N. Maraşli, Dependency of thermal conductivity on the temperature and composition of d-camphor in the neopentylglycol-d-camphor alloys, Thermochim. Acta. 531 (2012) 12–20. https://doi.org/10.1016/j.tca.2011.12.021.

[40] J. Shi, C. Tomasi, Good Features to Track, Proc. IEEE Conf. Comput. Vis. Pattern Recognit. (1994) 593–600. https://doi.org/10.1109/CVPR.1994.323794.

[41] MATLAB R2020b, Image Coordinate Systems, Image Process. Toolbox Doc. (2021). https://www.mathworks.com/help/images/image-coordinate-systems.html (accessed February 20, 2021).

[42] N. Otsu, A Threshold Selection Method from Gray-Level Histograms, IEEE Trans. Syst. Man. Cybern. 9 (1979) 62–66. https://doi.org/10.1109/TSMC.1979.4310076.

[43] Z. Jun, H. Jinglu, Image segmentation based on 2D Otsu method with histogram analysis, Proc. - Int. Conf. Comput. Sci. Softw. Eng. CSSE 2008. 6 (2008) 105–108. https://doi.org/10.1109/CSSE.2008.206.

[44] R. Trivedi, W. Kurz, Dendritic Growth, Int. Mater. Rev. 39 (1994) 49–73. https://doi.org/10.1179/095066094790326220.

[45] W.U. Mirihanage, K. V. Falch, D. Casari, S. McFadden, D.J. Browne, I. Snigireva, A. Snigirev, Y.J. Li, R.H. Mathiesen, Non-steady 3D dendrite tip growth under diffusive and weakly convective conditions, Materialia. 5 (2019). https://doi.org/10.1016/j.mtla.2019.100215.

[46] D. Walton, B. Chalmers, The Origin of the Preferred Orientation in the Columnar Zone of Ingots, Trans. Metall. Soc. AIME, Vol. 215. 215 (1959) 3–13.

[47] T. Takaki, S. Sakane, M. Ohno, Y. Shibuta, T. Shimokawabe, T. Aoki, Large-scale phase-field studies of three-dimensional dendrite competitive growth at the converging grain boundary during directional solidification of a bicrystal binary alloy, ISIJ Int. 56 (2016) 1427–1435. https://doi.org/10.2355/isijinternational.ISIJINT-2016-156.

[48] T. Takaki, M. Ohno, Y. Shibuta, S. Sakane, T. Shimokawabe, T. Aoki, Two-dimensional phase-field study of competitive grain growth during directional solidification of polycrystalline binary alloy, J. Cryst. Growth. 442 (2016) 14–24. https://doi.org/10.1016/j.jcrysgro.2016.01.036.

[49] T. Takaki, S. Sakane, M. Ohno, Y. Shibuta, T. Aoki, C.A. Gandin, Competitive grain growth during directional solidification of a polycrystalline binary alloy: Three-dimensional large-scale phase-field study, Materialia. 1 (2018) 104–113. https://doi.org/10.1016/j.mtla.2018.05.002.

[50] T. Takaki, S. Sakane, M. Ohno, Y. Shibuta, Competitive growth during directional solidification of a binary alloy with natural convection: Two–dimensional phase–field study, Model. Simul. Mater. Sci. Eng. (2019). https://doi.org/10.1088/1361- 651X/ab1a17.

[51] D. Tourret, A. Karma, Growth competition of columnar dendritic grains: A phase-field study, Acta Mater. (2015). https://doi.org/10.1016/j.actamat.2014.08.049.

[52] D. Tourret, Y. Song, A.J. Clarke, A. Karma, Grain growth competition during thin-sample directional solidification of dendritic microstructures: A phase-field study, Acta Mater. 122 (2017) 220–235. https://doi.org/10.1016/j.actamat.2016.09.055.